Bomb Strike Experiment for Mine Countermeasure

Dr. Peter C. Chu and LT Greg Ray
Naval Ocean Analysis and Prediction Laboratory, Naval Postgraduate School, Monterey CA 93943

Dr. Peter Fleischer
Naval Oceanographic Office, Stennis Space Center, MS 39529

Mr. Paul Gefken
SRI International, Menlo Park, CA

Abstract **- The Navy's bomb maneuvering model (STRIKE35) predicts the bomb location and trajectory in air and water columns. The Bomb Strike Experiment for Mine Countermeasure Operations, currently sponsored through the Office of Naval Research mine and obstacle breaching technology program, is part of a multi-year, comprehensive effort aimed at enhancing the Navy's fleet naval mine clearance capability and success. The investigation discussed in this thesis examines the experimental and theoretical characteristics of a rigid body falling through the air, water, and sediment column at high speed. Several experiments were conducted to launch bomb-like rigid bodies with the density ratio similar to operational munitions, namely the MK-84 general purpose bomb, into a hydrodynamic test tank. Careful observations of the bomb-like rigid body's position and orientation were collected and analyzed to produce a series of three-dimensional coordinate time-space data tables and plots. The resulting data set reveals a strong correlation between shape type and trajectory and dispersion patterns for rigid bodies moving through the water column at high velocity. This data will be used for development and verification of the three-dimensional model bomb strike model (STRIKE35) aimed at predicting the overall trajectory, maneuvering, burial depth and orientation of a falling high-velocity rigid body in the air-water-sediment column. The long-term goal of this project is to improve warhead lethality for use in quick, precise and accurate strikes on known enemy naval minefields in the littoral combat environment.**

1. Introduction

During the mid-1400's our world embarked on a journey of discovery as nations began reaching beyond their own borders to explore new lands and avenues of trade. Men like Columbus and Magellan led the hunt for new resources and markets, and sowed the beginning of the global economy we live in today. While many things have changed since those primitive beginnings, the ideas of international commerce and free trade between nations are as alive today as they were 600 years ago. Just as in the Age of Exploration, modern world trade is still primarily dependent on one factor - maritime transport.

Today, the vitality of the United States' economy relies on unencumbered trade and commerce over the world's ocean. According to the United Nations Conference on Trade and Development (UNCTAD), 2005 recorded yet another increase in the amount of goods traded globally by sea, raising the previous record to an all time high of 6.76 billion tons, an increase of 4.2% from the previous year (UNCTAD, 2005). At the top of these statistics stands the United States, which claims the title of the world's leading maritime trading nation, accounting for nearly 20% (measured in tons) of the annual world ocean-borne trade. A lynchpin of the American economy, this avenue of trade is responsible for 25% of the U.S. Gross Domestic Product (GDP), up from 11 percent in 1970, and experts agree that this figure will only continue to increase in coming years (Frittelli, 2004). The bulk of this trade is conducted by the 51,000+ vessels which ply the seas to service America's 360+ ports delivering approximately 90 percent of all cargo tonnage entering the country each year (Maritime Transportation Security Act of 2002). Clearly the importance of free access to the world's seas cannot be overstated with regard to its importance to the national welfare of the United States.

While sea-borne trade is acknowledged by experts to be the life blood of American commerce, the aftermath of the devastating attacks of September 11, 2001, has caused a shift in perspective as new assessments are made of these assets and their vulnerability to the possibility of similar attacks. Terrorist organizations are no longer viewed as unruly gangs of disgruntled militants, but rather highly-organized operatives working in conjunction around the world to accomplish a common objective. While much has been done in the last five years to thwart the functioning of terrorist training, planning and operational units, no one

Report Documentation Page

Form Approved
OMB No. 0704-0188

1. REPORT DATE	2. REPORT TYPE	3. DATES COVERED
2006		**00-00-2006 to 00-00-2006**

4. TITLE AND SUBTITLE	5a. CONTRACT NUMBER
Bomb Strike Experiment for Mine Countermeasure	5b. GRANT NUMBER
	5c. PROGRAM ELEMENT NUMBER
6. AUTHOR(S)	5d. PROJECT NUMBER
	5e. TASK NUMBER
	5f. WORK UNIT NUMBER
7. PERFORMING ORGANIZATION NAME(S) AND ADDRESS(ES) **Naval Postgruaduate School,Department of Oceanography,Monterey,CA,93943**	8. PERFORMING ORGANIZATION REPORT NUMBER
9. SPONSORING/MONITORING AGENCY NAME(S) AND ADDRESS(ES)	10. SPONSOR/MONITOR'S ACRONYM(S)
	11. SPONSOR/MONITOR'S REPORT NUMBER(S)

12. DISTRIBUTION/AVAILABILITY STATEMENT
Approved for public release; distribution unlimited

13. SUPPLEMENTARY NOTES
A National Oceanographic Partnership Program Award. Seventh Monterey International Symposium on Technology and Mine Problems, NPS, Monterey, California, May 1-4, 2006

14. ABSTRACT

15. SUBJECT TERMS

16. SECURITY CLASSIFICATION OF:			17. LIMITATION OF ABSTRACT	18. NUMBER OF PAGES	19a. NAME OF RESPONSIBLE PERSON
a. REPORT	b. ABSTRACT	c. THIS PAGE			
unclassified	**unclassified**	**unclassified**	**Same as Report (SAR)**	**18**	

really knows when or where terror will strike next. One thing is for certain, top security agencies agree that maritime transport is a prime candidate for future attacks. Given the strategic importance of maritime trade and commerce, the possibility of a major port or shipping facility within U.S. border becoming the focus of terrorist actions cannot be underestimated. What's more, is that though the Maritime Transport Act of 2002 called for a major increase in port security measures nationwide, the fact still remains that U.S. seaports are still highly vulnerable targets. Access to port facilities and shipping lanes are a critical link in the United States' economic chain and military mission, and the threat to these strategic venues from terrorist attach has never been greater (Frittelli, 2004).

2. The Naval Mine Threat

One of the most appealing weapons for use in paralyzing sea-borne trade and military operations is the naval mine. Naval mines today remain the perfect asymmetrical weapons, capable of disrupting assured access in areas of strategic importance to the United States and their Allies. Terrorists no doubt have examined the benefits of using naval mines, and in the hands of hostile forces, the relatively low-technology naval mine possesses a serious threats to global assured access of the world's oceans (Cornish, 2003)

The mine is an attractive weapon due to its availability, variety, cost-effectiveness, ease of deployment, and potential impact on naval operations (Department of the Navy, 2004). Possibly, the Committee for Mine Warfare Assessment expressed this best:

> Naval mines can be used strategically, channeling or denying passage through restricted waters and in and out of ports needed for sustenance by littoral nations. They can shape the naval battle space, the approaches to it, and routes of commerce, setting the conditions of a campaign. Used tactically, they can slow or stop movement to and through narrow straits and to landing zones on beaches, and in so doing can also make a slowed or stopped force more vulnerable. Yet despite the many instances in which mines were important in past conflicts, the U.S. Navy historically has underrated mine warfare as an element of naval warfare. (Naval Mine Warfare, 2001)

Every type of naval mine is available in the global marketplace, and most are affordable to almost anyone wishing to obtain one. Described by some as "A Poor Man's Naval Force", the most basic naval mine can be procured for just a few hundred dollars, deployed from virtually any air or water craft, and lie in wait until its target happens upon it location. It is not surprising therefore that mines have been the weapon of choice for nations and organizations that do not have the resources to develop and finance a navy that can challenge the United States. Naval mines are the perfect asymmetrical weapons, serving to level the playing field, offering an effective, low-cost counter to high-tech Navy's such at the U.S (Mitchell, 1999). To illustrate this point, Figure 1 depicts the damage inflicted on both men and platforms during recent armed encounters:

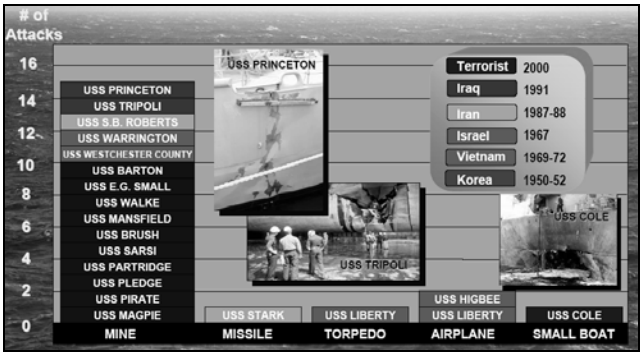

Figure 1. U.S. ship casualties by weapon type since 1950 (from Nash, 2005).

Cleary naval mines account for more casualties to U.S. ships than all other aggressor combined. To emphasize this even further consider the damage sustained by the three most recent targets of mine strikes (see Figure 2):

- 1988 - USS Samuel B. Roberts encountered a contact mine East of Bahrain which created a 6.5 m hole in the hull, busted the keel, dismounted the engines, and created a 50 m fireball in the air. The estimated cost of the mine was around $1,500 while the total cost for repair of the Roberts was around $135 million;
- 1991 - USS Princeton was struck by a Manta mine. The mine blast caused substantial damage including a cracked superstructure, severe deck buckling, and a damaged propeller shaft and rudder. The mine cost approximately $10,000 while repairs on the vessel totaled $24 million;
- 1991 - USS Tripoli encountered a LUGM-145, contact mine, lost a third of her fuel and cost $3.5M to repair.

In addition to severe casualties that mine encounters have had on the U.S. fleet, what makes naval mining even more significant is that even the psychological threat of using mines can threaten assured access to global water way. Rear Admiral Stephen Baker once remarked, "If you make an announcement that there are mines in the water, you've succeeded in 75% of your mission" (Johnson, 2003). The

major goal of naval mining is not focused on creating destruction or loss of life on the intended target, but rather to affect the timeline of movement for those vessels across the world's ocean. As stated, even the perceived threat of naval mines in a waterway will completely close those lanes of travel until mine hunting and sweeping operation can be completed days or weeks later. Whether a minefield is real or perceived it takes the same amount of time for Mine Countermeasure (MCM) forces to reopen the waterways. For this reason, the potential mining of U.S. waters must now be part of homeland defense priorities. Should a terrorist organization ever be successful in conducting a covert mining or perceived mining operation in a U.S. harbor the psychological effects would be enormous, and the port would be rendered completely ineffective halting all commerce in and out until MCM operations were completed. Because the United States relies so heavily on its ports and shipping for its economic vitality this would create a ripple effect into the economy creating a backlog of shipments, slowing the progress of industry and causing consumer prices to increase as access to goods becomes more difficult.

Figure 2. Mine Threat (from Cornish, 2003)

3. Organic Mine Countermeasure SYSTEMS

The goal of the navy regarding future MCM capability is to provide rapid, stand-off organic mine countermeasures capability to maintain assured access to the seas for both civil and military vessels. While historically MCM has been an afterthought on the warfare commander's battle plan, today more than ever military leaders are beginning to understand the implications of this threat, and are now taking a vested interest in developing a mine warfare force that is capable and responsive to 21st century threats.

Traditionally, meeting the MCM goal meant a long and tedious process, using a combination of mine hunting and sweeping techniques and equipment to locate, classify and neutralize naval mines. While effective, these operations are extremely time intensive and put personnel and equipment at severe risk. Today however, as depicted by Figure 3, much work is being done on the next generation of mine countermeasure technologies.

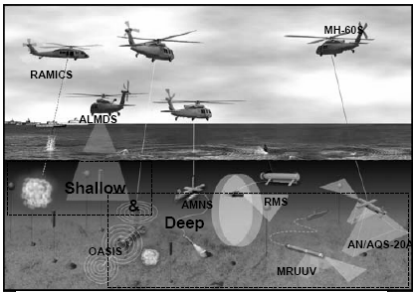

Figure 3. Future MCM systems (from Nash, 2005).

New platforms are such as the Airborne Mine Countermeasure aircraft (AMCM) and the JDAM Assault Breaching System (JABS) which will provide a stand-off MCM capability not yet seen in the warfare environment. Table 1 depicts current systems being developed for use in the organic mini countermeasure program.

MCM System	Description
AQS-20A Mine-hunting Sonar	Improved airborne mine hunting sonar with electro-optical identification capability for use on the AMCM SH-60S Helicopter
Airborne Mine Neutralization System (AMNS)	UUV deployed from an airborne platform to explosively neutralize sea mines previously located by mine hunting systems
Airborne Laser Mine Detection System (ALMDS),	Airborne LIDAR system used to detect, localize, and classify near-surface moored and floating mines
Rapid Airborne Mine Clearance System (RAMICS),	SH-60 mounted cannon fires 30 mm fin-stabilized discarding sabot rounds to detonate floating or moored mines detected by ALMDS
Organic Airborne and Surface Influence Sweep (OASIS) system	Self-contained, high speed, shallow water magnetic and acoustic influence sweeping device deployed from the helicopter to provide rapid mine clearance
Remote Mine-hunting System (RMS)	Long-duration, off board, unmanned vessel that can be employed from surface ships.
Mission Reconfigurable Unmanned Underwater Vehicle (MRUUV).	Modular UUV for submarine forces to provide assured access for submarine missions and intelligence preparation of the battle space for operational forces.
JDAM Assault Breaching System (JABS)	Joint Direct-Attack Munitions to disperse multiple explosives to destroy obstacles and mines on the beach and in the surf quickly.

Table 1. Overview of future MCM systems.

In addition to these systems, the vision of organic mine countermeasure warfare ensures that mine warfare will no longer be the responsibility of only a small number of dedicated professionals. The plan calls for all components of the naval force structure to possess awareness and an operational knowledge of mine warfare. Though the threat from naval mines will probably never completely disappear, when the vision for an integrated organic MCM force is realized, the United States and their Allies will at least have the ability to decrease the effectiveness of these

weapons and thus help prevent them from denying access to areas of strategic importance around the world.

4. Bomb Maneuver Modeling

This is a multi-year, comprehensive effort aimed at enhancing the Navy's fleet naval mine clearance capability and success. The multi-faceted program includes the following components: (1) Study of high-velocity rigid bodies falling through the air-water-sediment column using scaled models of current operational munitions, (2) development of bomb-strike prediction model (STRIKE35), (3) verification of STRIKE35 with full-size bomb striking exercises and (4) ensemble model development. This work is the extension of the current Office of Naval Research (ONR) sponsored program on mine and obstacle breeching technology. The investigation discussed in this paper addresses a component of this program by examining the experimental and theoretical characteristics of a rigid body falling through the air, water, and sediment column at high speed. Several experiments were conducted to launch bomb-like rigid bodies with the density ratio similar to operational munitions, namely the MK-84 general purpose bomb, into a hydrodynamic test tank. During the experiments, careful observations of the bomb-like rigid body's position and orientation were collected and analyzed to produce a series of three-dimensional Cartesian coordinate time-space data tables and plots. This resulting data will be used for numerical verification of the initial three-dimensional model (STRIKE35) aimed at predicting the overall trajectory, maneuvering, burial depth and orientation of a falling high-velocity rigid body in the air-water-sediment column.

The long-term goal of this project is to improve warhead lethality for use in quick, precise and accurate strikes on known enemy naval minefields in the littoral combat environment. (Chu et al, 2005) The MK-84 general purpose bomb was chosen as the prototype for modeling due to its current employment in the JDAM Assault Breaching System (JABS) (see Figure 4).

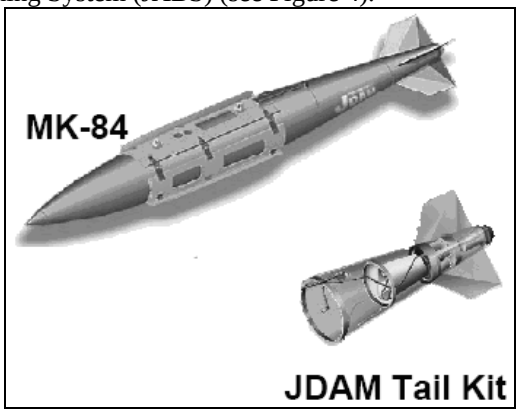

Figure 4. JDAM Assault Breaching System (JABS) (from Almquist, 2005)

Currently, JABS, developed by the Office of Naval Research, utilizes unitary bombs, fuses, and JDAM tail kits, as an interim solution for breaching surface laid minefields in the beach zones. The natural first step in expanding the JABS system would include employing it for use in clearing anti-invasion and various types of mines in the surf zone and very shallow water zone. Figure 4 depicts the types of threat and depth for each zone. If JABS is to be utilized as a mine countermeasure system for deeper water, further study and characterization of the system must be completed. The data collected in this project will serve to further this purpose and help make the JABS system a far more versatile tool in the MCM arsenal.

5. Hydroballistic Theory and Modeling

Recently, the scientific problem regarding the movement of a rigid body in the air-water-sediment column has drawn much attention to the area of naval research. This is primarily due to a heightened awareness of the sea mine threat to naval operations in our post-9/11 world. Quick, accurate and precise prediction of a fast-falling rigid body in the air-water-sediment column can greatly contribute to the overall effectiveness of utilizing bomb-strike operations for mine clearance in surf and very-shallow-water zones. Thus, the scientific significance and technical applications of such an investigation cannot be overstated.

The hydrodynamic characteristic of a rigid body provides for the utilization of up to six nonlinear equations, three momentum equations and three moment-of-momentum equations, for describing the general motion of the object. The scientific studies of the hydrodynamic characteristics of a rigid body in the air-water-sediment column involve nonlinear dynamics, body and multi-phase fluid interaction, body-sediment interaction, supercavitation and instability theory, while technical applications draw from a range of fields including aeronautics, navigation, and civil engineering.

A. Triple Coordinate Systems

Consider an axially symmetric cylinder with the centers of mass (**X**) and volume (**B**) on the main axis (Figure 5). Let (L, d, χ) represent the cylinder's length, diameter, and the distance between the two points (**X**, **B**). The positive χ-values refer to nose-down case, i.e., the COM is lower than the COV. Three coordinate systems are used to model the hydrodynamics of falling cylinder through the water column: E-, M-, and F-coordinate systems. All the systems are three-dimensional, orthogonal, and right-handed (Chu et al., 2004a).

The E-coordinate is represented by F_E(O, i, j, k) with the origin 'O', and three axes: *x*-, *y*- axes (horizontal) with the unit vectors (i, j) and z-axis (vertical) with the unit vector k

(upward positive). The position of the cylinder is represented by the position of the COM,

$$\mathrm{X}=x\mathbf{i}+y\mathbf{j}+z\mathbf{k}, \quad (1)$$

which is translation of the cylinder. The translation velocity is given by

$$\frac{d\mathbf{X}}{dt}=\mathbf{V}, \quad \mathbf{V}=(u,v,w). \quad (2)$$

Let orientation of the cylinder's main-axis (pointing downward) is given by $\mathbf{i}_M$. The angle between $\mathbf{i}_M$ and $\mathbf{k}$ is denoted by $\psi_2+\pi/2$. Projection of the vector $\mathbf{i}_M$ onto the (x, y) plane creates angle (ψ_3) between the projection and the x-axis (Figure 2). The M-coordinate is represented by $F_M(X, \mathbf{i}_M, \mathbf{j}_M, \mathbf{k}_M)$ with the origin '**X**', unit vectors ($\mathbf{i}_M$, $\mathbf{j}_M$, $\mathbf{k}_M$), and coordinates (x_M, y_M, z_M). In the plane consisting of vectors i_M and k (passing through the point M, called the IMK plane), two new unit vectors ($\mathbf{j}_M$, $\mathbf{k}_M$) are defined with j_M perpendicular to the IMK plane, and k_M perpendicular to i_M in the IMK plane. The unit vectors of the M-coordinate system are given by (Figure 2)

$$\mathbf{j}_M=\mathbf{k}\times\mathbf{i}_M, \quad \mathbf{k}_M=\mathbf{i}_M\times\mathbf{j}_M \quad (3)$$

The M-coordinate system is solely determined by orientation of the cylinder's main-axis i_M.

Let the cylinder rotate around ($\mathbf{i}_M$, $\mathbf{j}_M$, $\mathbf{k}_M$) with angles ($\varphi_1,\varphi_2,\varphi_3$) (Figure 2). The angular velocity of cylinder is calculated by

$$\omega_1=\frac{d\varphi_1}{dt}, \quad \omega_2=\frac{d\varphi_2}{dt}, \quad \omega_3=\frac{d\varphi_3}{dt}. \quad (8)$$

The F-coordinate is represented by $F_F(X, i_F, j_F, k_F)$ with the origin X, unit vectors (i_F, j_F, k_F), and coordinates (x_F, y_F, z_F). Let V_w be the fluid velocity. The water-to-cylinder velocity is represented by

$$\mathbf{V}_r=\mathbf{V}_w-\mathbf{V},$$

which can be decomposed into two parts,

$$\mathbf{V}_r=\mathbf{V}_1+\mathbf{V}_2, \mathbf{V}_1=(\mathbf{V}_r\cdot\mathbf{i}_F)\mathbf{i}_F, \mathbf{V}_2=\mathbf{V}_r-(\mathbf{V}_r\cdot\mathbf{i}_F)\mathbf{i}_F, \quad (12)$$

where $\mathbf{V}_1$ is the component paralleling to the cylinder's main-axis (i.e., along $\mathbf{i}_M$), and $\mathbf{V}_2$ is the component perpendicular to the cylinder's main-axial direction.

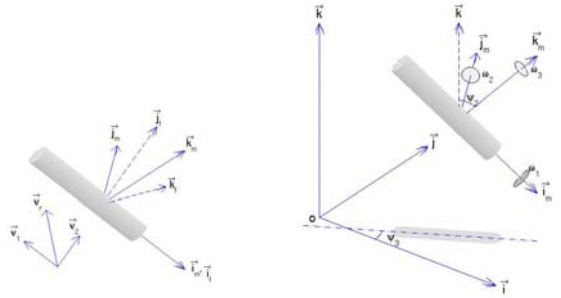

Figure 5. Three coordinate systems (from Chu et al., 2004).

B. Momentum Balance

The translation velocity of the rigid-body (V) is governed by the momentum equation in the E-coordinate system (Maxey and Riley, 1983)

$$\frac{d}{dt}\begin{bmatrix}u\\v\\w\end{bmatrix}=\begin{bmatrix}0\\0\\g(\rho_w/\rho-1)\end{bmatrix}+\frac{\rho_w}{\rho}\frac{D\mathbf{V}_w}{Dt}+\frac{1}{\rho\Pi}(\mathbf{F}_h+\mathbf{F}_V), \quad (7)$$

where g is the gravitational acceleration; $b=\rho_w g/\rho$, is the buoyancy force; ρ_w is the water density; Π is the cylinder volume; ρ is the rigid body density; $\rho\Pi$ = m, is the cylinder mass; V_w is the fluid velocity in the absence of the rigid-body at the center of volume to the body. F_h is the hydrodynamic force (including drag, lift, impact forces). The drag and lift forces are calculated using the drag and lift laws with the given water-to-cylinder velocity (V_r). In the F-coordinate, V_r is decomposed into along-cylinder (V_1) and across-cylinder (V_2) components. F_V is the force caused by bubble volume variation (bubble force).

C. Moment of Momentum Equation

It is convenient to write the moment of momentum equation,

$$\mathbf{J}\cdot\frac{d\boldsymbol{\omega}}{dt}=\mathbf{M}_w+\mathbf{M}_b+\mathbf{M}_h+\mathbf{M}_v, \quad (8)$$

in the M-coordinate system with the body's angular velocity components ($\omega_1,\omega_2,\omega_3$) defined by (4). Here, Mw is the torque due to the fluid acceleration $\rho_w/\rho D\mathbf{V}_w/Dt$. M_b is the torque due to buoyancy force $F_b = g(\rho_w/\rho-1)$. M_h is the hydrodynamic (drag and lift) torques. M_v is the torque due to the Basset history force. In the M-coordinate system, the moment of gyration tensor for the axially symmetric cylinder is a diagonal matrix

$$\mathbf{J}=\begin{bmatrix}J_1&0&0\\0&J_2&0\\0&0&J_3\end{bmatrix}, \quad (9)$$

where J_1, J_2, and J_3 are the moments of inertia. The gravity force, passing the center of mass, doesn't induce the moment.

D. Supercavitation

As a high-speed rigid body penetrates into the air-water interface, an air cavity will be formed. The shape of cavity is approximately elliptical. A number of scientists have developed formulas to predict the cavity radius such as the Logvinovich (1969) formula

$$r_{cav}=r_{\max}\sqrt{1-\frac{\left(1-r_1^2/r_{\max}^2\right)}{\left(1-t/t_m\right)^{2/\eta}}}, \quad (10)$$

where r_{max} is the maximum cavity radius; tm is the time for the formation of the cavity midpoint; η (~0.85) is the correction factor; and r_1 is the radius at location x_1; t is the time for the cavity formation at x_1,

$$t = \frac{x_M - x_1}{V_k}, \tag{11}$$

where V_k is the cavitator velocity. Recently, Dare et al. (2004) proposed a simpler formula from experimental studies

$$r_{cav} = \frac{d}{2}\sqrt{\frac{kx_M}{d} + 1}, \tag{12}$$

where k = 2 and d is the nose diameter. The shock propagation and subsequent bubble formation may be significantly affected by the presence of an air cavity around the rigid-body. Supercavitation often occurs around the body. Cavitating flows are usually described by the cavitation number,

$$\sigma = \frac{p - p_v}{\frac{1}{2}\rho_w V_w^2}, \tag{13}$$

where p is the hydrostatic pressure, p_v is the pressure in the cavity. For supercavitating flow the cavitator is located at the forward most location on the body, and the cavity downstream of the cavitator covers the body. The shape of the cavity is defined by the cavitation number. The aspect ratio (length L versus diameter dm) is the function of cavitation number

$$\lambda = \frac{L}{d_m} = \frac{\sigma + 0.008}{\sigma(0.066 + 1.7\sigma)} \tag{14}$$

Several expressions can be used for the drag coefficient. Without considering the geometry of cavity, the cavitator drag coefficient is simply calculated by (Stinebring et al., 2001)

$$C_d = 0.82(1 + \sigma). \tag{15}$$

With considering the geometry of cavity is considered, the cavitator drag coefficient is expressed by

$$C_d = \left(\frac{2r_{cav}}{d}\right)^2 (\sigma - 0.132\sigma^{8/7}) \tag{16}$$

E. Bubble Dynamics

Drag due to bubble volume variation is calculated by (Johnson and Hsieh, 1966)

$$\mathbf{F}_V = 2\pi r_b^2 \rho_w (\mathbf{V}_w - \mathbf{V}) \frac{dr_b}{dt} \tag{17}$$

where r_b is the bubble radius. The Rayleigh-Plesset equation (Plesset, 1948)

$$r_b \frac{d^2 r_b}{dt^2} + \frac{3}{2}\left(\frac{dr_b}{dt}\right)^2 = \frac{1}{\rho_w}(p_v - p_g \frac{\Pi_{b0}}{\Pi_b} - p - \frac{2\tau}{r_b} - \frac{4\mu}{r_b}\frac{dr_b}{dt}), \tag{18}$$

where p_g is the initial partial pressure of the non-condensable gas; Π_{b0} is the initial volume of the bubble; Π_b is the volume of the bubble; τ is the surface tension; and μ is the dynamic viscosity of water.

F. Model Scaling

Ensuring proper similitude between prototype and 1/12 model is key to successful physical modeling. For true scaling the prototype must be geometrically, dynamically and kinematically similar to the prototype. Of primary concern are effects of the inertial, gravitational, and viscous forces that act on the model as it travels through the water column. Unfortunately, when using water as both the test and prototype medium, it is impossible to satisfy the requirements for gravitational and viscous scaling simultaneously. The hydroballistic model must therefore be designed to scale one force ratio and minimize the other. (Waugh et al, 1973) In this case gravity is regarded as a second order force, and the emphasis is placed on the handling the interaction between the inertial and viscous forces.

Kinematic viscosity is related to the drag coefficient and the Reynolds number. The Reynolds number, R_e, is the ratio of the inertial to viscous forces.

$$R_e = \frac{\rho V d}{\mu}, \tag{19}$$

where ρ is the density of the fluid, V is the velocity scale, d is the model diameter, and μ is the kinematic viscosity of the fluid. To achieve similitude between the scale model and the prototype, R_e must be equal in both.

Figure 6 depicts the relationship between drag coefficient and the Reynolds number for a given set of flow parameters around a 5.1 cm circular cross-section (Gefken, 2005).

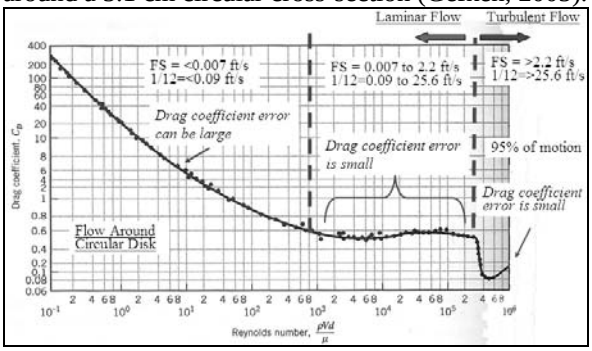

Figure 6. Drag coefficient versus Reynolds number (From: Gefken, 2005)

Of primary interest in Figure 6 is the region where the Reynolds numbers exceed $4x10^3$. This region is characterized by a turbulent flow regime. Because the drag coefficient tends to be very small in this area, this is where the model and prototype Reynolds numbers will most closely match and similitude will be at its greatest. The velocity threshold for remaining in the region of turbulent flow is approximately 7.8 m/s. Thus, for the model bombs to conform to the Reynolds scaling regime velocities must meet or exceed this minimum level. When the model velocity drop below this point the flow regime begins transitioning from turbulent to laminar flow and the similitude between the model and prototype begins to degrade.

6. Bomb Strike Experiment

A. Preparation

The overall premise of the bomb strike experiment consists of inserting various bomb-like test shapes into water, and recording their underwater trajectory over the course of the flight path. Data collection was facilitated by a pair of high-speed video cameras mounted below the water surface. Following the data collection phase of the project, all video trajectory data was converted into an array of Cartesian coordinate points which will serve as the initial data set for the development and validation of the bomb-strike prediction model (STRIKE35).

A1. Hydrodynamic Test Shapes

A collection of four bomb-like polyester resin test shapes were used during the experiment phase of the project. These shapes consisted of a right-cylinder, right-cylinder with hemispheric nose cone (capsule), scale model of the MK-84 GP munitions (bomb) and a modified version of the model bomb which had no stabilizing fins (shell).

The construction of the test shapes consisted of a three part production process: prototype development, mold construction and test shape casting and finishing. This process was necessary to facilitate more efficient experimentation and to reduce the production cost of the experimental test shapes.

Prototype production began with the development of a 1/12 scale replica of the real-world operational MK-84 GP bomb. This initial prototype was machined from aluminum alloy stock based on known dimensional characteristics. To create the cylinder and capsule prototypes, a polyester resin casting was created by pouring liquid plastic into a 2" PVC mold. The shapes were allowed to cure, and then were machined to their final dimensions. As these two shapes were not intended to mimic any type of real-world munitions, their dimensions were based solely on similarity to the 1/12 scale model bomb. The final prototype created was the shell shape. Construction of this design consisted of creating a polyester resin casting of the bomb prototype. The shape was then machined and sanded to remove the fins, and produce the final prototype shape. Diagrams of the final prototypes with dimensions are depicted in Figure 7 and Table 2:

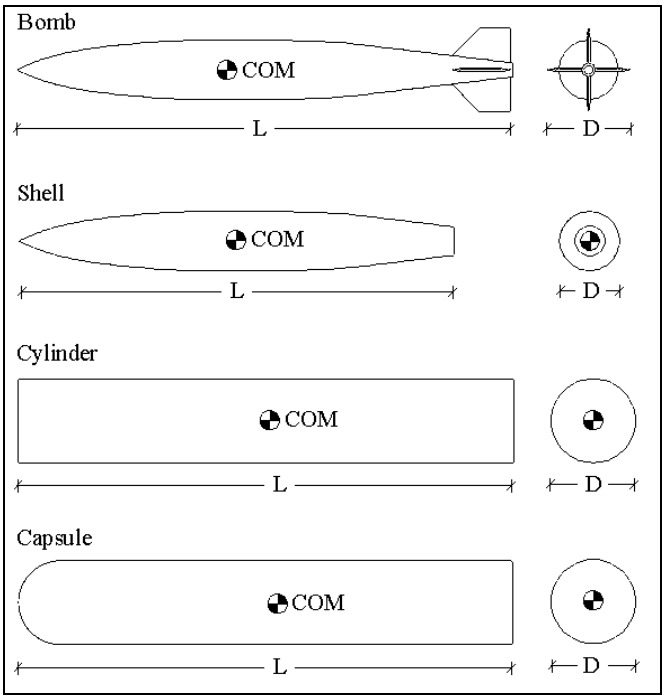

Figure 7. Model Prototype Diagram

	Length L – (cm)	**Diameter** D – (cm)	**Total Mass** (g)	COM – (cm)	**Specific Gravity** (g/cm^3)
Full Scale Bomb	382.3	58	941.95kg	160.3248	2.3
1/12 Scale Model					
True Scale	31.85	4.83	545.2	13.3604	2.3
Actual Model	31.85	4.83	563.4	13.75	2.224
% Error	0	0	3.3	2.9	3.3
Other Shapes					
Shell	27.94	4.02	473	14.2	2.224
Cylinder	31.75	5.18	831	16.08	1.754
Capsule	31.75	5.18	808	15.95	1.754

*Center of mass measured from nose of model shape

Table 2. Model Characteristics Table.

Once prototype construction was complete, work began on making casting molds of the prototypes from which the final experimental shapes could be produced. Mold production was identical for all four shapes. The

mold making process consisted of making two separate mold halves for a given shape. To create the first half of the mold, a cardboard container was constructed to hold the shape and the molding materials. This container was sealed at all joints, and then filled 2/3 with sand. On top of the sand, a layer of modeling clay was packed and smoothed in the container. The prototype shape was then depressed half way into the clay along its long axis leaving the remaining half of the shape exposed (Figure 8). To facilitate simple removal from the final mold, the exposed portion of the shape, clay and interior of the container were coated with a silicon release agent. After all preparations were complete, the remainder of the box was filled with commercially available liquid urethane rubber molding compound and allowed to cure overnight. It is also worth noting that the particular type of urethane rubber used is of the sort which did not require vacuum degassing to remove bubbles. When the rubber was cured into its final state, the completed mold-half was removed from the container. To create the second half of the mold, the process was repeated, but instead of using sand and clay to support the prototype, the newly created mold half was utilized. After the entire mold was complete (Figure 9), holes were placed in the ends of the mold to facilitate resin insertion and the evacuation of air as the casting material entered the mold. This process was repeated for all remaining prototype test shapes.

The final step in the production of the testing shapes consisted of pouring and finishing the numerous uniform-density polyester resin castings created from the prototype molds. The castings were created from commercially available, two-part, ultra-low viscosity, rigid, urethane casting resin which readily accepts coloring and density additives and yielded virtually bubble-free castings without costly degassing procedures. As possibility of damage to the test facility and personnel was of paramount concern, the resin chosen possessed a shore hardness rating of 70D which means that the shape would maintain dimensional integrity throughout the flight path, but still pose little risk of damage to the facility were it to impact the wall, window or floor of the test tank at high velocity.

Figure 8. Prototype in mold box prior to adding mold rubber compound

Figure 9. Finished rubber MK-84 model mold.

To facilitate creation of an accurately scaled model, all portions of the resin mixture were carefully measured and weighed, and fine brass powder was added to the resin during mixing to achieve the proper density ratio. When all materials were prepared, the rubber mold was coated with silicone release agent, and closed using cloth straps. The resin mixture was then poured into the mold (Figure 10) and allowed to cure overnight.

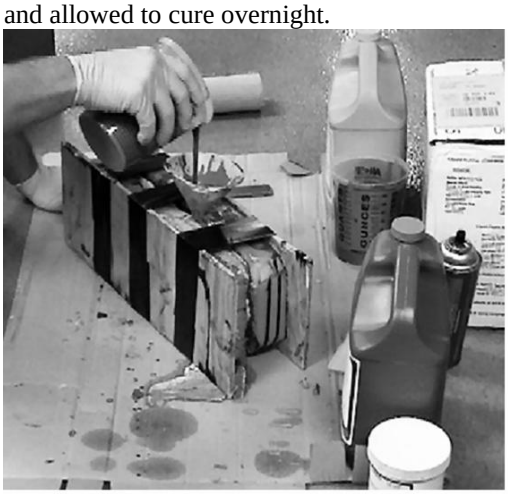

Figure 10. Pouring the resin mixture into the model mold.

When the casting was fully cured, the mold was carefully opened, and the final testing model removed from the mold. The models were allowed to cure an additional 48 hours prior to finishing. Finishing consisted of filling any imperfections with a slurry of polyester resin, followed by sanding and painting. All models were painted with flat black spray enamel, and a series of white fiducials were added to aid in analysis of the digital video data (Figures 11). This process was repeated for each category of prototype so that at the time of experimentation, there were six testing models of each test shape available.

(a)

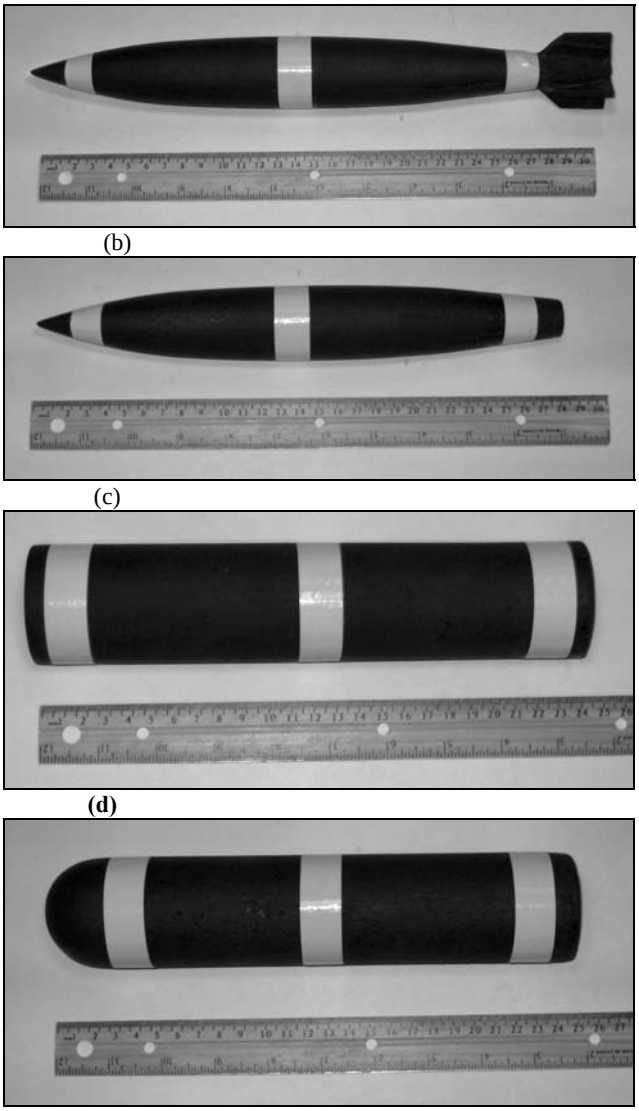

(b)

(c)

(d)

Figure 11. (a) MK-84 bomb models with 1/12 scale, (b) shell test model, (c) cylinder test model, and (d) capsule test model.

A2. Pneumatic Launching Device

To facilitate the high-velocity portion of the experiment, a pneumatic launching device was created to propel the test shapes into the water at a rapid entry speed. The launcher was primarily constructed of schedule 40 polyvinylchloride piping (PVC). The device consisted of three primary components: air chamber, valve mechanism, breech-load firing barrel (Figure 12).

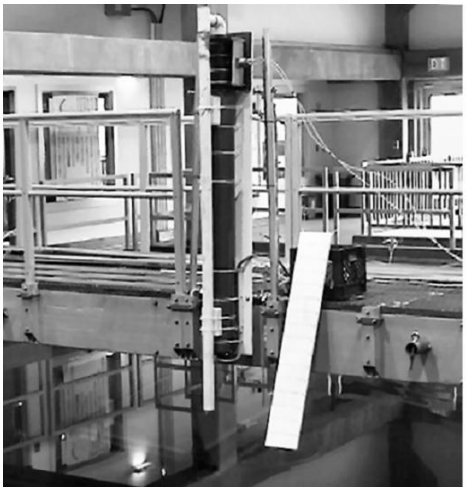

Figure 12. Pneumatic launcher mounted on bridge

The air chamber was constructed of a single, five foot section of 6" PVC. The chamber was sealed on the end with a standard 6" end cap, and then connected to the valve mechanism via a series of PVC reducer bushings. A standard 2" PVC ball valve was fitted between the air chamber and firing barrel, and served to maintain the chamber in a pressurized state until triggered. When actuated, the valve instantaneously opened releasing the pressurized volume of air into the firing barrel. Because of the high pressures experienced by this valve, a hydraulic actuator was fitted to the device to provide the motive force necessary to open the valve. The final portion of the launcher consisted of a firing barrel. This barrel had a removable cap on the closed end to facilitate efficient reloading of the test shapes. Small foam sabots with fine wire lanyards (Figure 13) which extended through a pinhole in the removable loading cap provided the means by which test shapes were held in the barrel until fired.

The launcher was mounted to a steel frame oriented vertically downward with the end of the barrel positioned orthogonal to the water surface at a height of 12 inches above the water. The entire apparatus was secured to the tank bridge by lag bolts and ratchet tie down straps (Figure 14). Additional equipment associated with launcher included a pressure indicator, emergency release valve, pneumatic fill and triggering mechanism and a 120 p.s.i. air source.

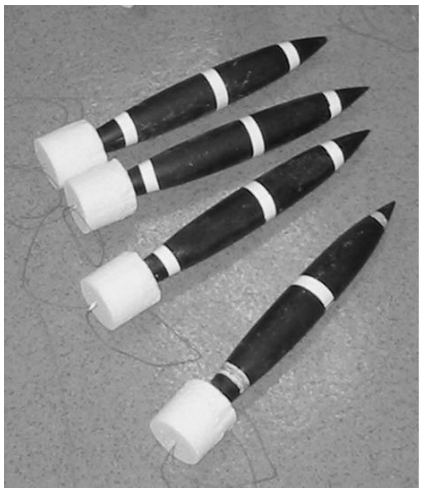

Figure 13. Models fitted with foam sabots and wire lanyards

A3. Hydrodynamic Test Facility

The bomb strike experiment was conducted at the Monterey Bay Aquarium Research Institute (MBARI) Unmanned Underwater Vehicle Test Tank. This tank was used to simulate the near-shore environment frequently experienced in real-world mine countermeasure operations. The facility consists of a 30' x 45' x 30' tank filled with standard sea water, and is contained inside a large building which provided shelter from wind and elements. A sliding bridge spans the width of the tank, and was used as a mounting surface for the pneumatic launcher and lighting equipment. Eight viewing windows located approximately six feet below the water surround the tank, and provided a venue for unimpeded sub-surface data collection to a scaled depth of roughly 120 feet. The conditions of the tank were maintained via an ozone filtration system, and aside from the remnants of blue dye placed into the tank several weeks prior to the experiment, the tank was free from contaminates at the beginning of the experiment. It is of worth noting at this point, that while the dye did not affect the hydrodynamic characteristics of the test shapes, it did significantly impact the ability to properly illuminate the tank, and hence the quality of the video data was somewhat degraded. Figure 15 detail the characteristics of the facility.

In addition to the previously mentioned equipment and facilities, a large test shape recovery device was assembled and installed in the tank prior to testing. This apparatus consisted of a 30' x 40' net attached to a PVC grid-framework constructed of ¾" piping. The entire apparatus was inserted horizontally across the water, and was used to recover shapes between testing runs using a series of weights and pulleys located in the corners of the tank to raise and lower the device. Lastly, two large blue tarps were placed in the tank against the walls centered in each camera's field of view. This provided a solid contrasting background which assisted in the analysis phase of the project in distinguishing the falling shapes from the environment around them.

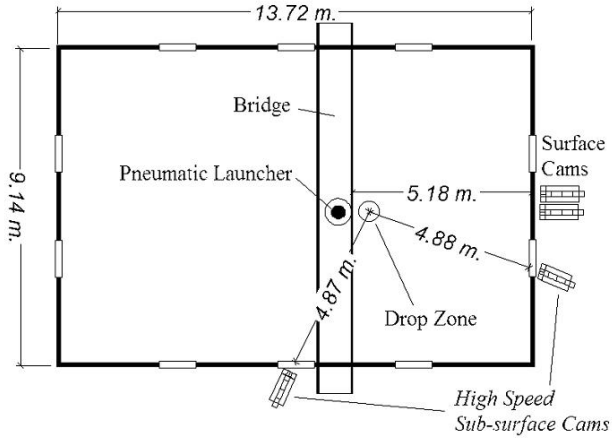

Figure 14. Test Facility Plan View

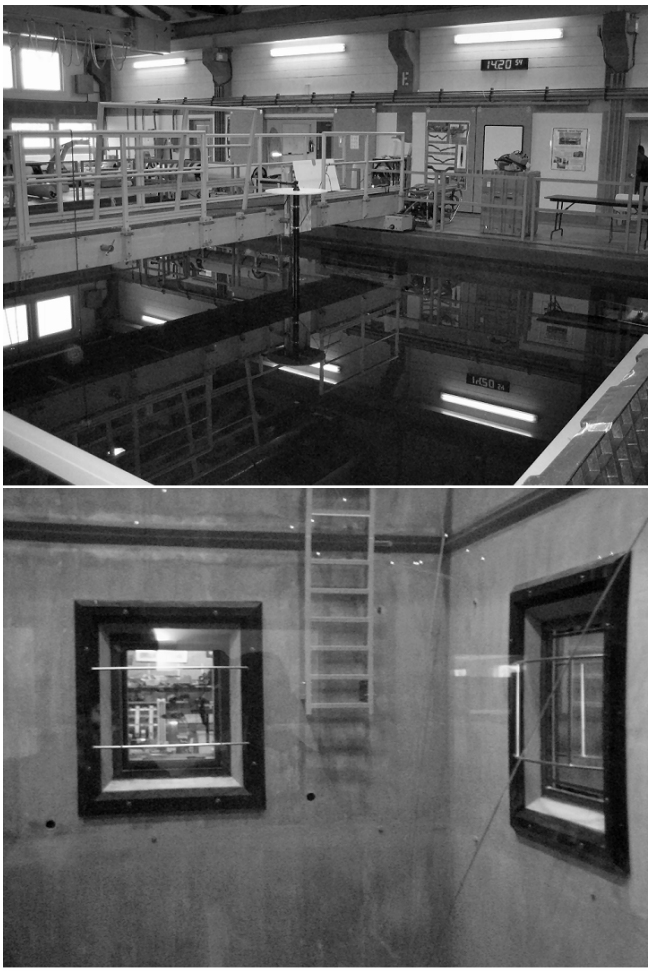

Figure 15. Test tank - above surface (upper panel), below surface (lower panel).

A4. Data Collection Equipment

All data was collected digitally using a network of high-speed and standard video equipment and computers. Surface level information collected included experiment data and the video log. This data was collected using a pair of standard commercially available digital video camera, mounted on tripods, and located at the end of the pool directly in front of the testing zone. Both cameras operated at a 30Hz frame rate. The data camera used a narrow view lens zoomed to focus on the area directly between the launcher and the water surface, and was toggled on and off between test runs. Data from this camera was later used to ascertain the initial velocity of the shapes as they entered the water. The second camera used a wide angle lens, and was employed to record a video log of the experiment. This device ran continuously throughout the experiment.

Below surface video imagery, used to determine the trajectory of the falling shapes, was collected using a pair of high-speed, Photron FASTCAM PCI digital cameras (Figure 16). These cameras were mounted on tripods in two separate windows, at an angle of 70 degrees in relation to one another so as to provide two, near orthogonal, views of the drop zone. After mounting and calibration, each camera station was covered with black plastic to block out any light source beside that which came from the field of view. The cameras were time-synchronized, calibrated and connected by a centrally located laptop computer via high-speed data cables. During testing the cameras were operated using the Photron FASTCAM Viewer software at 512 x 480 pixel resolution at full frame and recording rates of 125 Hz. To facilitate a wider field of view, both cameras were fitted with wide angle lens. All data was recorded digitally on a standalone 200GB hard drive during the test phase. Additionally, to enhance the quality of the data, during testing the installed tank lighting system was turned to its maximum setting and a pair of 1000 watt high intensity photography lights were mounted and used above the surface.

B. Methodology

The bomb-strike experiment consisted of a series of low velocity and high-velocity runs of the four testing shapes which were launched vertically into the water. The entry of each shape into the water was recorded by the two above surface video cameras. This above-surface data was then digitally analyzed using 2-D motion analysis software to determine the initial velocity of all shapes. All below-surface data collection was facilitated by the two FASTCAM PCI high-speed cameras. The below-surface digital data was analyzed by 3-D motion analysis software to determine the trajectories of each shape. All data from runs which involved malfunctions was discarded.

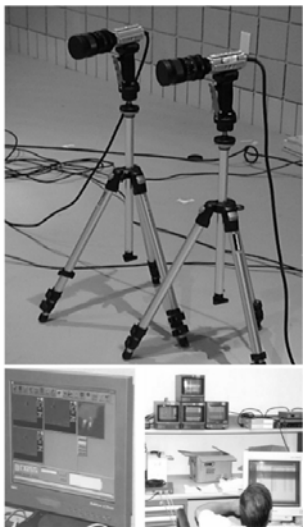

Figure 16. Camera and analysis hardware and software.

C. Camera Calibration

Prior to the commencement of testing, calibration images were taken from each underwater camera view. This procedure provided an artificial frame of reference for use by the analysis software in computing the shape's trajectory in the data retrieval phase. To accomplish this task, a geo-referenced calibration target (Figures 17-18) consisting of a white, three-dimensional cross was lowered into the camera's field of view to a depth of 100 inches and filmed. The z-axis was determined by the vertical component of the cross, and the two horizontal components were used to acquire the x and y axis. Following acquisition of all calibration images, both cameras were secured to their final position and barricaded to prevent disturbance during the testing phase.

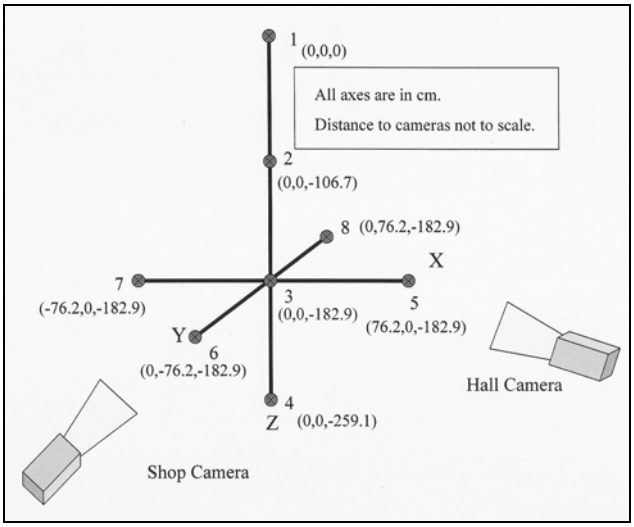

Figure 17. Calibration cross diagram

D.Testing Procedures

The overall project was a two-man job conducted via handheld walkie-talkies. One man remained on or near the moveable bridge and was responsible for loading the launcher, toggling the lights and above-surface cameras and performing the launch. The other man was stationed with the high-speed cameras and computer, and served to coordinate the filming and retrieval of the below-surface data. For each individual drop, the experimenter below confirmed the readiness of the high-speed cameras and prepared the computer to save the appropriate film file. When this was confirmed, he signaled the man above, who performed the launch.

After a coordinated count conducted via the walkie-talkies, the man at the launch position fired the launcher as the man below began filming the test run. When the shape passed through the field of view of both cameras, the camera operator would cease filming, save the appropriately named file, and again signal the man above, who would then turn off the lighting and note the time and shape in the experimental record notebook. The cycle would then repeat itself until all shapes were fired. Recovery of the shapes was as described above. Digital imagery data obtained in the experiment was then analyzed to generate water trajectory data and graphics.

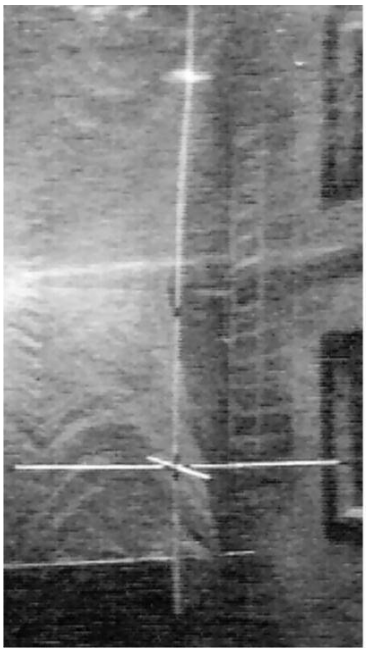

Figure 18. Underwater view of calibration cross

7. Data Retrieval and Analysis

A. Overview

The data retrieval and analysis phase of the project was a multi-step process which employed various software applications and analysis techniques to produce the final data set. Figure 19 depicts the general steps in this process.

B. DATA RETRIEVAL

The experimental phase yielded a total of 43 movie sets, each consisting of a pair trajectory movies produced from the two sub-surface high-speed cameras. Figure 20 depicts the flight path of a bomb model as viewed from the two near-orthogonal high-speed cameras.

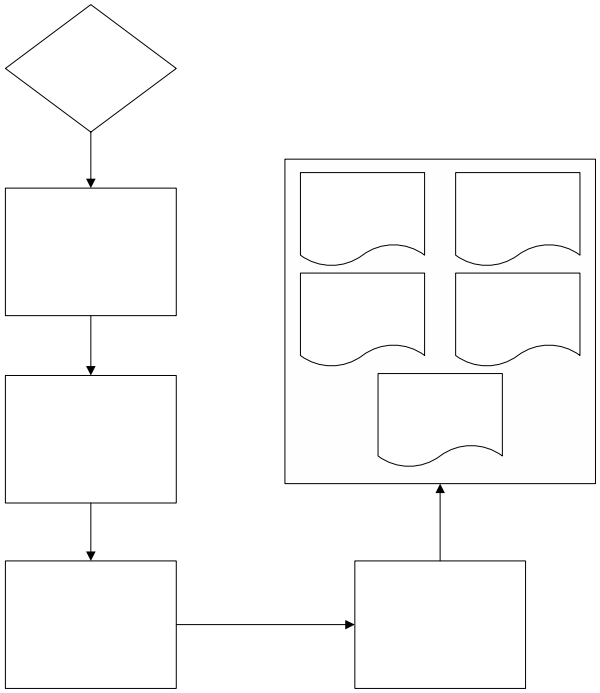

Figure 19. Data retrieval and analysis diagram

(a)

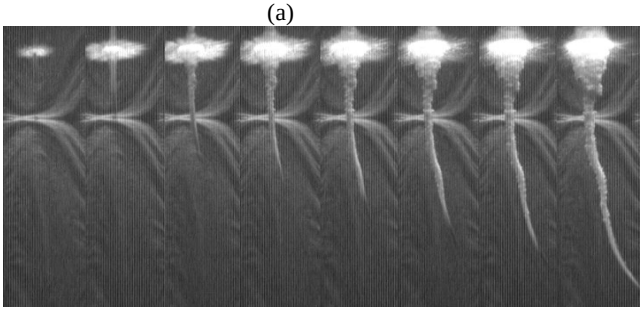

(b)

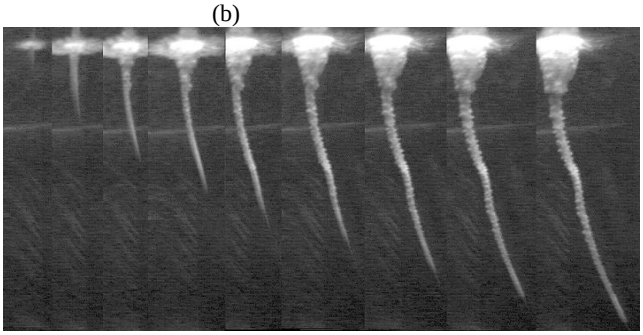

Figure 20. Model bomb trajectories from (a) Camera # 1, and (b) Camera #2.

For each test run, each pair of two dimensional movies were combined into a single three dimensional array of x-y-z coordinate data. Commercially available 3-D motion analysis software was the primary tool utilized to perform this function. Initially, the software was calibrated (Figure 21) into the 3-D coordinate reference system utilizing the pairs of calibration images obtained in the initial phase of the experiment.

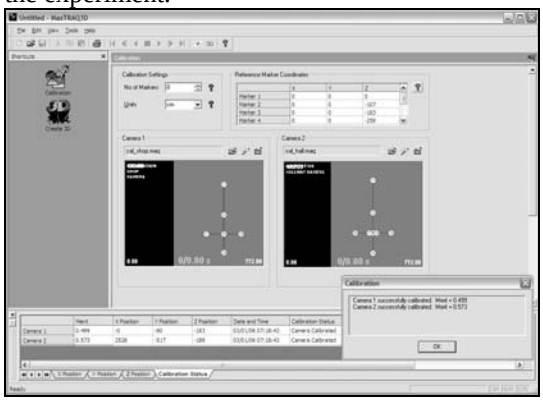

Figure 21. Software screenshot – camera calibration

Following calibration, both camera views were time synced and analyzed to determine the actual position of the shape in the x-y-z coordinate field. Frame-by frame analysis (Figure 22) was performed with the software for each view by manually identifying and inputting a pair of marker points associated with the test shape's position. The markers were generally linked to the shape's leading and trailing edges, however in frames where an edge was not visible, the position of the marker was estimated visually based on the previous and subsequent viewable frames.

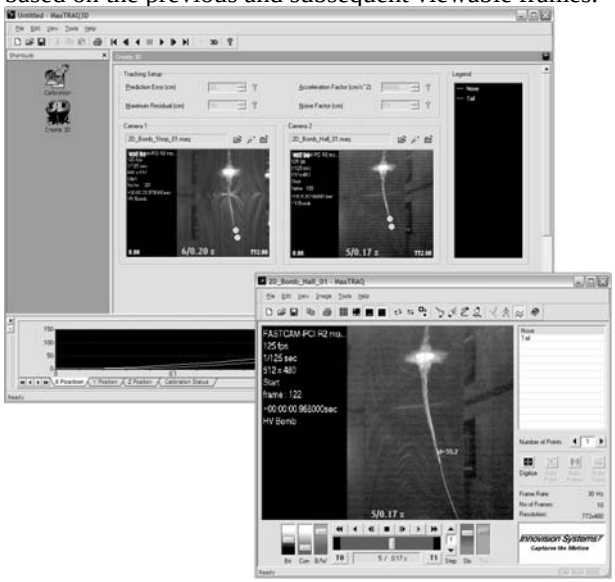

Figure 22. Software screenshot – digital retrieval of trajectory data

Following the digitization of data for both views, the automated functions of the software were employed to compile the 2-D images into a calibrated array of 3-D positional data. This data was saved in an electronic database for use in the final motion analysis and modeling phase of the project.

C. DATA ANALYSIS

The three-dimensional coordinate array from each test run was analyzed using the MATLAB software suite. The primary focus of the MATLAB routine was to compute the midpoint between the nose and tail points on the model, and determine the elevation and azimuth of the shape at a given point in order to describe it's maneuvering characteristics as it fell through the water column. The application was also employed to generate all data plots. In total, for each test run the analysis routine produced three trajectory plots (x-z, y-z, x-y-z) (Figure 23) and one dispersion plot at 2.5 m depth (Figure 24).

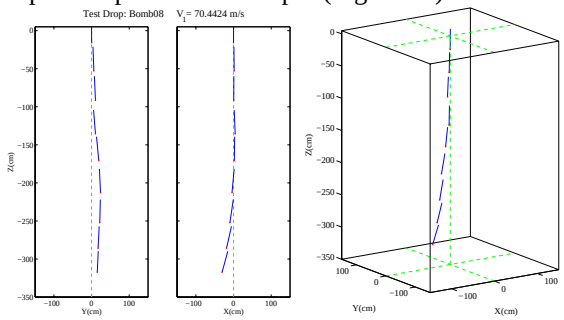

Figure 23. Model bomb tracks obtained using MATLAB.

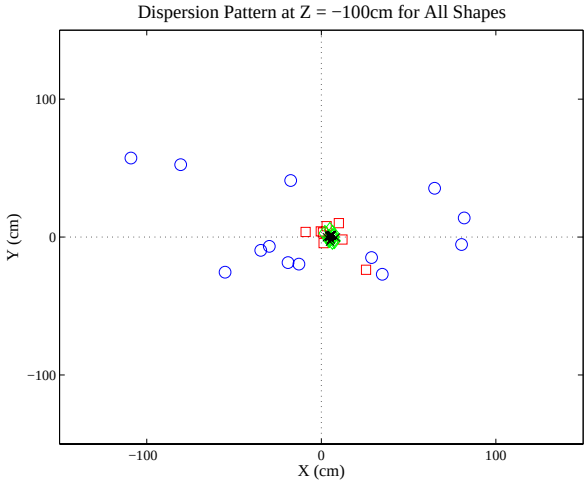

Figure 24. Dispersion of model bombs at 2.5 m depth.

8. Results

A. Trajectory Patterns

The primary purpose in conducting the Bomb Strike Experiment was to determine the water-phase trajectory pattern of bomb-like rigid bodies while falling through the water column at high velocities. To accomplish this task, combination of model MK-84 bombs and other

hydrodynamic test shapes were launched into water at high rates of speed. Upon analysis of the video data collected from the 43 test runs, four generalized trajectory patterns were formulated to categorize the maneuvering characteristics of the model shapes. These generalized trajectory patterns are described in Table 3 and Figure 25.

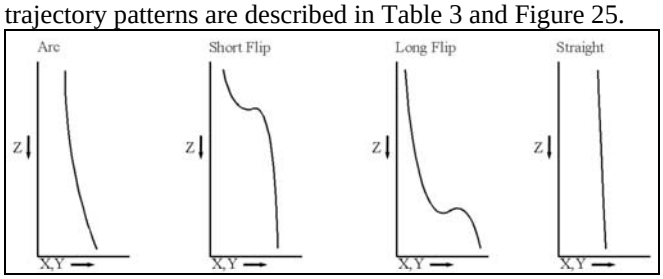

Figure 25. Generalized trajectory patterns.

Trajectory Pattern	Description
Arc	Slow gradual curve along the vertical axis throughout the duration of the trajectory pattern
Short Flip	Quick, abrupt turn towards the water surface during initial 100cm of underwater flight followed by slow gradual decent to terminus of trajectory pattern usually characterized by tail-first or near-horizontal model orientation,
Long Flip	Gradual curve until final 1/3 of flight then characterized by rapid, abrupt turn towards the surface followed by slow gradual decent to terminus of trajectory pattern.
Straight	Generally straight or slanted flight path with very little curvature along the vertical axis throughout trajectory pattern.

Table 3. Generalized trajectory pattern descriptions.

B. Dispersion Patterns

In addition to compiling the trajectory plots, the data was also analyzed to investigate the dispersion patterns of the shapes at various z-levels as they fell through the water column. The z-level chosen were 25 cm, 100 cm, and 250 cm. These depths were chosen as scaled representations of the actual depths of real-world mine warfare littoral zone classifications. The 25 cm depth represents the bottom of the real world surf zone, 100 cm depth represents the bottom of the Very Shallow Water Zone and the 250cm depth represents the middle of the Shallow Water Zone. The dispersion plots are a plan view depicting the shape distribution on the X-Y plane at a given z-level. The plot is divided into four quadrants to facilitate classification of each shape at that z-level. Figure 26 provides an example of the combined dispersion plot at 250 cm. Table 4 summarizes the trajectory patterns of all 43 test runs conducted during the Bomb Strike Experiment.

Table 4. Summary of experimental results.

Run ID	Initial V (m/s)	Travel Time (s)	Dispersion Quadrant	Trajectory Pattern
Bomb01	59.6398	0.064	1	Arc
Bomb02	42.5558	0.072	3	Straight
Bomb03	87.091	1.936	1	Erratic
Bomb04	69.4836	0.064	1	Arc
Bomb05	73.0189	0.064	1	Arc
Bomb06	66.9995	0.064	2	Arc
Bomb07	67.5673	0.064	2	Arc
Bomb08	70.4424	0.064	2	Arc
Shell01	29.156	1.928	2	Erratic
Shell02	48.5448	0.368	4	Short Flip
Shell03	49.7667	2.224	2	Short Flip
Shell04	84.0531	1.4	4	Short Flip
Shell05	109.4761	1.68	3	Short Flip
Shell06	65.32	1.72	3	Short Flip
Shell07	91.7885	1.84	1	Short Flip
Shell08	74.7778	1.12	3	Short Flip
Shell09	64.7494	1.68	3	Short Flip
Shell10	84.3337	1.92	1	Short Flip
Shell11	90.6474	1.56	3	Short Flip
Shell12	74.3143	1.44	1	Short Flip
Shell13	93.8647	3.16	3	Short Flip
Capsule01	56.1691	0.608	1	Long Flip
Capsule02	72.2632	0.608	3	Long Flip
Capsule03	77.8575	0.736	2	Long Flip
Capsule04	62.3611	0.568	1	Long Flip
Capsule05	87.418	0.264	4	Long Flip
Capsule06	64.5469	0.712	3	Long Flip
Capsule07	57.4379	0.48	1	Long Flip
Capsule08	83.1899	0.44	1	Long Flip
Capsule09	63.7256	0.768	1	Long Flip
Capsule10	69.1012	0.4	3	Long Flip
Capsule11	65.164	0.4	3	Long Flip
Cylinder01	28.157	0.368	1	Straight
Cylinder02	40.7162	0.376	0	Straight
Cylinder03	52.6362	0.336	1	Straight
Cylinder04	44.0899	0.448	0	Straight
Cylinder05	50.6464	0.296	4	Straight
Cylinder06	65.2215	0.256	4	Straight
Cylinder07	67.9315	0.256	4	Straight
Cylinder08	54.7307	0.68	0	Straight/Erratic
Cylinder09	53.4531	0.288	1	Straight
Cylinder10	58.2447	0.32	2	Arc
Cylinder11	56.9073	0.648	o	Long Flip

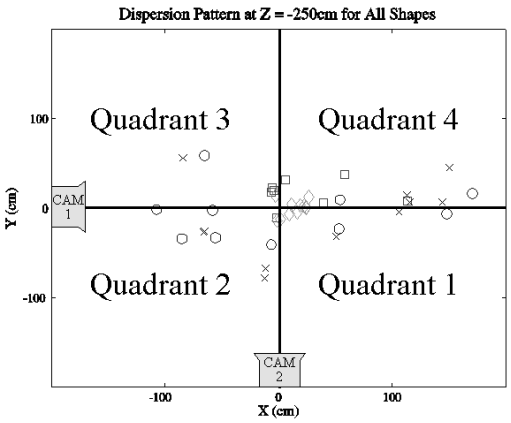

Figure 26. Example dispersion plot with camera placement and quadrant designation

C. Trajectory Patterns

The trajectory patterns of each model type were noticeably affected by the size and shape of the models themselves. The four shape types exhibited marked differences in there water phase trajectories. More than any other factor these differences appeared to be linked to three factors: shape of the nose cone, location of center of gravity and the presence or absence of stabilizing fins. To begin looking at the trajectory patterns it must be stated that by and large, the four generalized patterns were not shared among the various shapes, but rather, they were quite consistent within each shape type.

The simplest shape, the cylinder, was the most predictable and stable shape of all. Out of a total of eleven test runs, nine of the shapes exhibited an almost vertical trajectory pattern from the point of water entry to the terminus of the flight path. Like all other shapes, the cylinder was launched orthogonal to the water's surface with initial velocities ranging from 28 m/s to 67 m/s. The major determining factor in the shape's trajectory appeared to by the flat plate nose. As the shape entered the water, the uniform surface maintained constant pressure on the water preventing the development of under pressure or the whip phenomenon which caused other shapes to veer off course.

The next most complex shape in the series is the capsule shape. The capsule and cylinder are almost identical shapes in terms of density, mass, and center of gravity, however the capsule replaces the cylinder's flat plate nose cone with a hemispherical nose cone. In 100% of the test runs, this modification appears to have been the causative agent in the long-flip style trajectory classification. With everything else remaining the same, the differences in trajectory pattern between the cylinder and the capsule are undeniably linked to the hemispherical nose cone on the capsule. Also likely to have played a role in the more dynamic trajectory pattern is the location of the center of gravity. The center of gravity is located further to the rear of the shape thus increasing the propensity for the shape to flip at lower velocities.

The last two shapes, the bomb and the shell, differed widely from the previous two examples, and also from each other. The bomb shape displayed the arc trajectory pattern during 75% of the test runs. This pattern was characterized by a slow and gradual arc along the vertical axis. The stabilization effects of the tail fins kept the bomb stable throughout the flight path. Additionally, the tapered nose and tail minimized the cavitation bubble which allowed for a more steady-trajectory pattern. Alternatively, the shell shape demonstrated a very erratic trajectory pattern. As the shell entered the water and the came in contact with the water surrounding the bubble plume, the drag created on the side of the shape caused it to make an abrupt turn towards the surface before descending tail first to terminus of the pattern. This attribute was likely attributed to the lack of tail fins in conjunction with the flipping tendency caused by the rearward oriented center of gravity.

Of special interest to the bomb shape was Bomb Test #3. During this particular test run the model experienced tail slap when entering the water, and as a result lost all tail fins. The ensuing flight path was extremely erratic, characterized by a tumbling action as it progressed through the water column. This shape was completely unpredictable and followed a flight path unlike the other shapes. The unexpected loss of the stabilizing fins demonstrated the amount of chaos that can occur when the model shape malfunctions.

Overall, it can be concluded that the variance in trajectory patterns was primarily a result of the various model shapes and their center of gravity. While the trajectory patterns changed dramatically from shape to shape, they remained fairly constant within a particular shape type.

D.Layered Dispersion Patterns

The primary purpose of determining the dispersion pattern for each group of shapes was to provide a measured view of the amount of spreading that occurs as different shape types move downward through the water column. Since the experiment was conducted on $1/12^{th}$ scale, the z-levels chosen were able to represent various layers in the real-world littoral combat zone. These z-level represented various depths in the water column where forces might be conducting MIW operations. Figure 27 depicts the munition types and layer depths for these zones.

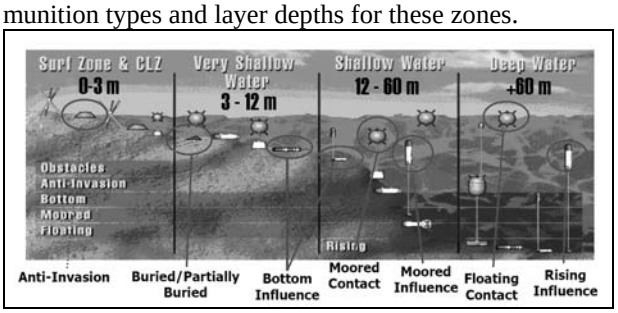

Figure 27. Littoral combat zones and munitions (After: Nash,

2005)

The scaled levels chosen for the dispersion plots were z = 25cm, z=100cm and z=250 cm serving as 1/12 scale representations of the 0-3m Surf Zone, 3-12m Very Shallow Water Zone and the 12-60 m Shallow Water Zone respectively. It is within these zones where 99% 0f mine warfare operations are conducted.

The result from these plots are depicted in Appendix B, and show a significant variance in spreading from one shape type to another as the z-level becomes deeper. For the z=25 cm case, 86% of shapes fall within a 5cm radius of the origin of the drop. The six shapes falling outside of this 10% radius zone are all shell type shapes which have previously been shown to exhibit the most aggressive trajectory pattern. At z=100cm, the spreading increases further, however 68% of all shapes remain within the 10% boundary borders. In this case the all but one of the shells has exceeded this border, and a few bomb shapes are beginning to venture away from the origin. Finally, at the z=250cm level, the spreading of all shapes is at its fullest. Only 47% of all shapes remain within 25 cm of the origin. All bombs, shells and capsules are widely spread in the dispersion pattern. The only shape that remains consistently near to the origin is the cylinder. This shape never exceeds a distance from the origin greater than 10% of the overall z-level. It stays tightly packed near the center of the field of view for its entire flight path. This is most likely due to the simplicity of the shape which decreases the interaction with the water, and thus prohibiting it from veering off course.

E. Sources of Error

Several known sources of error existed during the Bomb Strike Experiment which served to hinder the overall data gathering and analysis process. Using unfamiliar and untested techniques and equipment was a primary source of delay in the experimental and analysis phase of the project, and likely contributed to the existence of several error sources.

The primary known error was found in the data collection phase of the project. Filming in an underwater environment introduces many inherent difficulties which can serve to degrade the quality of data. Add to this the complication of filming at high-speed and the problem of collecting useable data becomes even more difficult. One area of error associated with the underwater filming stems from the parallax and distortion caused by filming an object in one medium while the cameras are in another medium. This distortion was minimized, however, by using special lenses and correction software in conjunction with the calibration methods described previously.

The use of high-speed cameras also introduced shape position tracking difficulty. The increased frame rate associated with high-speed filming necessitated much brighter lighting in the test tank than was available during the experiment. While the water appeared bright and clear on low-speed film, it was much darker in the 125 Hz video image. This effect was compounded by the remnants of blue dye that were still in the water from a previous experiment weeks earlier. The low brightness made distinguishing the black bomb shape from the background more difficult. The darkness problem could not be counteracted, and hence, some frames of each drop were difficult to process.

The air cavity and bubble plume generated by the pneumatic launcher and the shape itself greatly also hindered the ability to view and digitize the trajectory data. As the air cannon is actuated a volume of air is pushed ahead of the model shape as it moves down and out of the firing barrel. This air creates a depression in the water surface causing distortion of the field of view. Additionally, a shape entering the water also generates its own air cavity. That air cavity affects both the initial motion of the shape in the water, and also the visibility of that shape as the bubble plume collapses around the shape during flight. The air cavity effect on the motion was minimized by the high initial velocities. However, the bubbles from the cavity prohibited automatic tracking via software. In some frames, the test shape was completed obscured and had to be estimated based on the position of the shape in the surrounding frames.

The last known source of error stems from model production errors. First, unlike the actual prototype bomb shape, the 1/12 scale model bomb were created as uniform density shapes made from a polyester resin and brass mixture. As such, the shapes displayed geometrical similarity and the same average density as the real-world prototypes, however the shapes did not realistically detail the inner structure, electronics, or explosive distribution of their counterparts. Furthermore, during the resin curing process, the denser brass powder within the mixture may have “settled” somewhat in the molding process. Attempt to minimize this effect were taken by regularly rotating the molds during the hardening process, but settling inevitably occurred resulting in slightly-unsymmetrical mass distribution that affected the trajectory results. Overall the model bomb shapes were very similar to the prototypes, but these inherent errors did cause the center of gravity for the models to be slightly altered from the prototype to a measure of less than 3% error overall.

9. Conclusions

The first phase of the Bomb Strike Experiment Project has successfully demonstrated and characterized the physical and theoretical hydroballistic characteristics of high-velocity bomb-like rigid bodies as they move through the air-water-sediment column. Through careful observation of the shape’s position and orientation during the underwater trajectory phase, a large data set consisting of three-dimensional Cartesian coordinate trajectory arrays for various modeled bomb-like shapes was compiled. One of

the most difficult challenges faced in this project was ensuring proper scaling of the models to the prototypes, and this was also completed with a high degree of success.

The most striking result from the Bomb Strike Experiment was found in the correlation of trajectory and dispersion patterns which were unique to each shape type. All shape type demonstrated a very consistent trajectory and dispersion characteristics which was unlike the patterns displayed in the other shapes. The cylinder shape was the most consistent shape, with 100% of all test runs displaying the straight path trajectory pattern and tight grouping at each z-level for the dispersion analysis. In contrast to this, stands the shell shape type which demonstrated repeated erratic behavior for each run. This pattern was displayed by all shell shapes, and was characterized by an abrupt turn towards the surface followed by a slow descent to the terminus of the flight. As a result of this trajectory pattern the shell shape displayed the widest s-reading at all z-level on the dispersion plots. The unique patterns within each shape type lead to the conclusion that trajectory and dispersion is primarily dependent on the physical characteristics of shapes entering the water. Each shape type displayed a pattern consistent for its geometry which provides a very positive outlook for the prospect of accurate predicting the trajectory and dispersions of shapes in numerical modeling.

Future work in this multi-faceted project should include first and foremost the development and numerical verification of an initial three-dimensional model (STRIKE35) aimed at predicting the overall trajectory, maneuvering, burial depth and orientation of a falling high-velocity rigid body in the air-water-sediment column. Further investigations should include more in-depth study and verification of the modeled data with testing of full size high velocity rigid-body hydroballistics. Eventually, following initially numerical modeling and verification efforts, an emphasis should be placed on integrating the STRIKE35 model into ensemble models which can be deployed and utilized by forces in an operational environment.

Overall, 43 bomb-like shapes were launched into the water, compiling over 120,000 frames of video data, which was eventually translated into almost 60,000 3- dimensional trajectory data points making this one of the most comprehensive data gathering effort thus far in naval mine warfare modeling. While much work is still necessary to transform this project into operational use, this experiment has set the course for the STRIKE35 modeling efforts for many years to come, and advances the goal of improving warhead lethality for use in quick, precise and accurate strikes on known enemy naval minefields in the littoral combat environment is now one step closer.

Acknowledgments.

This study was supported by the Naval Oceanographic Office (contract numbers: N6230604PO00123, N6230605PO00223) and Office of Naval Research (grant numbers: N0001405WR20209, N0001406WR20076).

REFERENCES

Arnone, R.A., and Bowen, Prediction Model of the Time History Penetration of a Cylinder through the Air-Water-Sediment Phases. NCSC Letter Report T34, Naval Coastal Systems Center, Panama City, FL, 1980

Baciocco, A.J., Jr., Technology for the United States Navy and Marine Corps, 2000-2035: Becoming a 21st Century Force, Undersea Warfare, Volume 7. National Academy of Sciences, 1997. (http://www.nap.edu/html/tech_21st/uw2.htm)

Brown, J., Mine Warfare Brief, Defense Technical Information Center. (http://www.dtic.mil/ndia/expeditionary/brown.pdf) 30 January 2006

Chu, P.C., V. Taber, and S.D. Haeger, Environmental Sensitivity Study on Mine Impact Burial Prediction Model. Proc. of the Fourth International Symposium on Technology and the Mine Problem, April 2000, Naval Postgraduate School.

Chu, P.C., A.F. Gilles, C.W. Fan, J. Lan and P. Fleischer, "Hydrodynamics of falling cylinder in water column," *Adv. Fluid Mech.*, 4, 163-181, 2002a.

Chu, P.C., T.B. Smith and S.D. Haeger, Mine impact burial prediction experiment. *Proceedings on the Fourth International Symposium on Technology and the Mine Problem***,** Naval Postgraduate School, 10 pp., CD Rom, 2002b.

Chu, P.C., C.W. Fan, A. D. Evans, A.F. Gilles, and P. Fleischer, Three-dimensional hydrodynamic model for prediction of falling cylinder through water column. DVD-ROM, The OCEANS 2003 MTS/IEEE Conference Proceedings, San Diego, CA, Sept. 22-26, 2003.

Chu, P.C., C.W. Fan, A.D. Evans, and A.F. Gilles, Triple coordinate transforms for prediction of falling cylinder through the water column. *J. Applied Mech.*, 71, 292-298, 2004a.

Chu, P.C., C.W. Fan, and A. D. Evans, "Three-dimensional rigid body impact burial model (IMPACT35)," *Adv Fluid Mech.*, 6, 43-52. 2004b.

Chu, P.C., A.D. Evans, A. F. Gilles, T. Smith and V. Taber, "Development of Navy's 3D mine impact burial prediction model (IMPACT35)," *Proceedings on the Sixth International Symposium on Technology and the Mine Problem***,** Naval Postgraduate School, 10 pp., DVD-ROM, 2004c.

Chu, P.C., A. F. Gilles and C.W. Fan, Experiment of falling cylinder through the water column. *Exper. Thermal Fluid Sci.*, 29, 555-568, 2005a.

Chu, P.C., and C.W. Fan, Prediction of falling cylinder through air-water-sediment columns. *J. Appl. Mech.*, in press 2005b.

Chu, P.C., and C.W. Fan, Pseudo-cylinder parameterization for mine impact burial prediction. *J. Fluids Eng.*, 127, 1515-1520, 2005c.

Chu, P.C., C.W. Fan, A.D. Evans, A. Gilles, T. B. Smith, and V. L. Taber, Development and Verification of 3D Mine Impact Burial Prediction Model (IMPACT35). IEEE J. Oceanic Eng., in revision, 2006.

Crowe, C.T., J.A. Roberson and D.F. Elger, *Engineering Fluid Mechanics*, 7th Ed., John Wiley & Sons Inc, New York, 714 pp, 2001.

Department of the Navy. U.S. Naval Mine Warfare Plan Fourth Edition, Programs for the New Millenium. Washington, D.C., January 2006. (http://www.exwar.org/Htm/ConceptDocs/Navy_USMC/MWP4thEd/appendix_a.htm) 30 January 2006

Elmore, P.A., R. Wilkens, T. Weaver and M. D. Richardson, IMPACT 28 and 35 simulations of 2003 Baltic Sea cruise: model results and comparison with data. *Fifth Annual ONR Workshop on Mine Burial Prediction*, Kona, Hawaii, Jan 31 - Feb 2, 2005.

Gefken, P., 1/12-Scale Mk84 Model Testing. *8th Joint Classified Bombs/Warheads and Ballistics Symposium*, Monterey, California, Aug. 18, 2005.

Gilles, A., Mine Drop Experiment (MIDEX). *Master Thesis*, Naval Postgraduate School, Monterey, CA, 2001 (Advised by P.C. Chu).

Holland, K.T., A.W. Green, A. Abelev and P.J. Valent, "Parameterization of the in-water motions of falling cylinders using high-speed video," *Experi. Fluids*, 37, 690-770, DOI 10.1007/800348-004-0859-2, 2004.

Hurst, R.B., Mine Impact Burial Prediction Model – Technical Description of Recent Changes and Developments. Defense Scientific Establishment, Auckland, New Zealand, Report 149.

Knudsen, T., The Use and Development of Sea Mines, NDRF Summer Conference, 27 August 2004. Powerpoint Presentation.
(http://www.nrdf.dk/documents/groupp/SS04-Knudsen.pdf) 30 January 2006

Lott, D.F., K. Williams, and D. Jackson, Mine Burial in Carbonate Sediments. Proc. of the Technology and Mine Problem Symposium, November 1996, Naval Postgraduate School.

Von Mises, R., *Theory of Flight*, 1st Ed., Dover Publications Inc., New York, 564-585 pp., 1959.

Satkowiak, L.J., User's Guide for the Modified Impact Burial Prediction Model. NCSC TN 884-87. Naval Coastal Systems Center, Panama City, FL, 1987.

Smith, T.B., Mine Burial Impact Prediction Experiment. *Master Thesis*, Naval Postgraduate School, Monterey, CA, CA, 2000 (advised by P.C. Chu).

Taber, V.L., Environmental Sensitivity Study on Mine Impact Burial Prediction Model. *Master Thesis*, Naval Postgraduate School, Monterey, CA, 1999 (advised by P.C. Chu).

White, F.M., *Viscous Fluid Flow*, McGraw-Hill Inc., New York, 712 pp., 1974.